Submacropulse electron-beam dynamics correlated with higher-order modes in a Tesla-type cryomodule

A. H. Lumpkin,* R. Thurman-Keup, D. Edstrom, P. Prieto, and J. Ruan
Fermi National Accelerator Laboratory, Batavia, Illinois 60510, USA

B. Jacobson, J. Sikora, J. Diaz-Cruz,† A. Edelen, and F. Zhou
SLAC National Accelerator Laboratory, Menlo Park, California 94720, USA

(Received 16 October 2021; accepted 23 May 2022; published 24 June 2022)

Experiments were performed at the Fermilab Accelerator Science and Technology facility to elucidate the effects of long-range wakefields in TESLA-type superconducting rf cavities. In particular, we investigated the higher-order modes (HOMs) generated in the eight, nine-cell cavities of a cryomodule (CM) due to off-axis steering with correctors located ∼4 m upstream of the CM. We have observed correlated submacropulse centroid slews of a few hundred microns and centroid oscillations at ∼240 kHz in the rf beam-position-monitor data after the CM. The entrance energy into the CM was 25 MeV, and the exit energy was 100 MeV with 125 pC/bunch and 400 pC/bunch in 50-bunch pulse trains. These experimental results were evaluated for machine learning training aspects which will be used to inform the commissioning plan for the Linac Coherent Light Source-II injector CM. With an entrance beam energy of < 1 MeV in this case (or for ∼6 MeV at the European X-ray Free-electron Laser injector), the HOM-effect mitigation would be particularly critical.

DOI: 10.1103/PhysRevAccelBeams.25.064402

I. INTRODUCTION

The preservation of the low emittance of electron beams during transport in the accelerating structures is an ongoing challenge for large facilities. In the cases of the TESLA-type superconducting rf cavities currently used in the European X-ray Free-electron Laser (EuXFEL) [1] and the under-construction Linac Coherent Light Source Upgrade (LCLS-II) [2], off-axis beam transport may result in emittance dilution due to transverse long-range wakefields (LRWs) and short-range wakefields (SRW) [3–5]. To investigate such effects, experiments were performed at the Fermilab Accelerator Science and Technology (FAST) facility with its unique configuration of two TESLA-type cavities after the photocathode rf gun followed by an eight-cavity cryomodule [6]. Previously, we reported beam dynamics studies in regard to the single TESLA-type cavities for LRWs [4] and SRWs [5], but here we extend the LRW techniques to a full eight-cavity cryomodule for the first time. In addition, we also obtained detailed spectrally resolved HOM data with a high-resolution oscilloscope using the FFT of time-domain data. This enabled us to track the 18 individual dipolar modes in the first two passbands *including phase and mode polarization effects* [7].

We generated beam trajectory changes with the corrector magnet set located 4 m upstream of the cryomodule and observed correlations of the cavity higher-order modes' (HOMs) signal levels and submacropulse centroid slews and/or centroid oscillations in the 11 beam-position-monitor (BPM) locations downstream of the cryomodule. At 125 pC/bunch, 50 bunches per macropulse, 25-MeV entrance energy, and 100-MeV exit energy, we observed for the first time submacropulse position slews of up to 500 microns at locations within 3.59 m after the CM and a centroid oscillation at a difference frequency of 240 kHz further downstream. Both are emittance-dilution effects which we mitigated with selective upstream beam steering. The experiments were facilitated by the implementation of two prototype HOM detector chassis designed for the LCLS-II injector cryomodule. These chassis were based on the basic Fermi National Accelerator Laboratory (FNAL) design with a dipolar mode passband and zero-bias Schottky detectors, and they had additional selectable features for up to two wideband amplifiers in series and attenuators in each channel [8]. The combined eight channels then enabled signal acquisition from one coupler of all eight cavities at the same time to assess the beam trajectory relative to the cavity-mode centers. We did not

*lumpkin@fnal.gov
†Also at University of New Mexico, Albuquerque, New Mexico 87131, USA.

pursue actual high-resolution beam-position data with multiple methods on a single bunch in a third-harmonic module as in Zhang *et al.* [9], but we uniquely identified *submacropulse* beam-centroid slew and oscillations correlated with HOMs in a cryomodule as complementary information. In addition, we fielded a hybrid HOM detector box that selectively filtered the raw signal at two additional frequency bands centered at 2.5 and 3.25 GHz. These hybrid boxes also had raw, filtered outputs which were used with the high-speed oscilloscope to assess steering effects and resolve frequency splitting of the two-mode polarizations in the two different cavity structures from two vendors and also confirmed the steering optimizations.

Further, as a developmental activity, we used the steering-dependent HOM and rf BPM data for machine learning (ML) training in regard to minimization of HOMs and reduction of emittance dilution effects in a CM [10]. This result will be relevant to LCLS-II injector commissioning where < 1 MeV beam will be injected into the first cryomodule with the gradients of the first three cavities being 8, 0, and 0 MV/m and the last five cavities at 16 MV/m [11]. Wakefield kicks to the beam go inversely as beam energy so steering on axis into these first cavities will be crucial to avoid emittance dilution [4,5].

II. EXPERIMENTAL ASPECTS

A. The FAST electron linac

The Integrable Optics Test Accelerator (IOTA) electron injector at the FAST facility (Fig. 1) begins with an L-band rf photoinjector gun built around a Cs_2Te photocathode (PC). When the UV component of the drive laser, described elsewhere [12], is incident on the PC, the resulting electron bunch train with a 3-MHz micropulse repetition rate exits the gun at 4.5 MeV. Following a short transport section with a pair of trim dipole magnet sets, the beam passes through two superconducting rf (SCRF) capture cavities denoted CC1 and CC2 and then a transport section to the low-energy electron spectrometer. In this case, this dipole power is off so a 25-MeV beam is transported to the CM with an exit energy of 100 MeV. The beam parameters are shown in Table I. The micropulse or bunch (b) numbers were either 1 or 50. Diagnostics used in these studies included the rf BPMs (Bnnn) in the beamline (plus the cold BPM at the downstream end of the CM) and the detectors viewing the HOM coupler signals from the upstream (US) and downstream (DS) ends of each of the eight SCRF cavities as shown in Fig. 1.

TABLE I. Summary of the electron beam parameters used in the CM studies. The rf power is pulsed with a macropulse rate of 1–5 Hz.

Parameter	Units	Value
rf gun energy	MeV	4.5
Beam energy	MeV	25–100
Micropulse repetition rate	MHz	3
Micropulse No.	⋯	1–50
Charge	pC	10–500
Emittance (normalized)	mm mrad	2–5
Bunch length (rms)	ps	10–15
CC1 rf gradient	MV/m	21
CC2 rf gradient	MV/m	0
CM:Cn gradient	MV/m	∼9.5

The rf BPM electronics with data acquisition provides the centroid of each micropulse or bunch in an array file as well as the average position over the whole pulse train [13]. The BPM number and position for horizontal and vertical axes are denoted BnnnPH and BnnnPV, respectively. This array data is of course critical to display any submacropulse centroid oscillations or slewing that we correlate with the difference frequency of the HOM and a beam harmonic of the 3-MHz-repetition-rate pulse train.

For completeness, a schematic of the TESLA nine-cell, a 1300-MHz cavity is provided in Fig. 2(a) with the location and orientation of the two HOM couplers at either end indicated [14]. The azimuthal angles were proscribed differently as shown in Fig. 2(b) for the two couplers as a compromise on damping dipolar modes and their two polarization components [15]. The trajectory of the beam is indicated by the arrow and the offset x, and angle α is indicated. The induced net dipolar fields such as in Fig. 2(c) are proportional to the charge, R/Q, and more strongly with the offset than an angle [16]. In our experiments, we have used a single set of correctors to adjust the beam angle

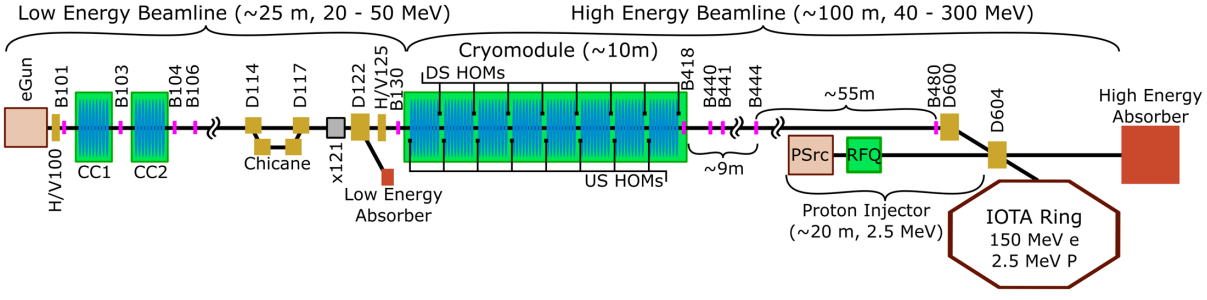

FIG. 1. FAST Linac showing the locations of the rf PC gun, CC1 and CC2 single cavities, the rf BPMs (Bnnn), the H/V125 correctors, the cryomodule CM2 with 8 cavities and 16 HOM couplers, and high-energy beamline. This schematic is not to scale.

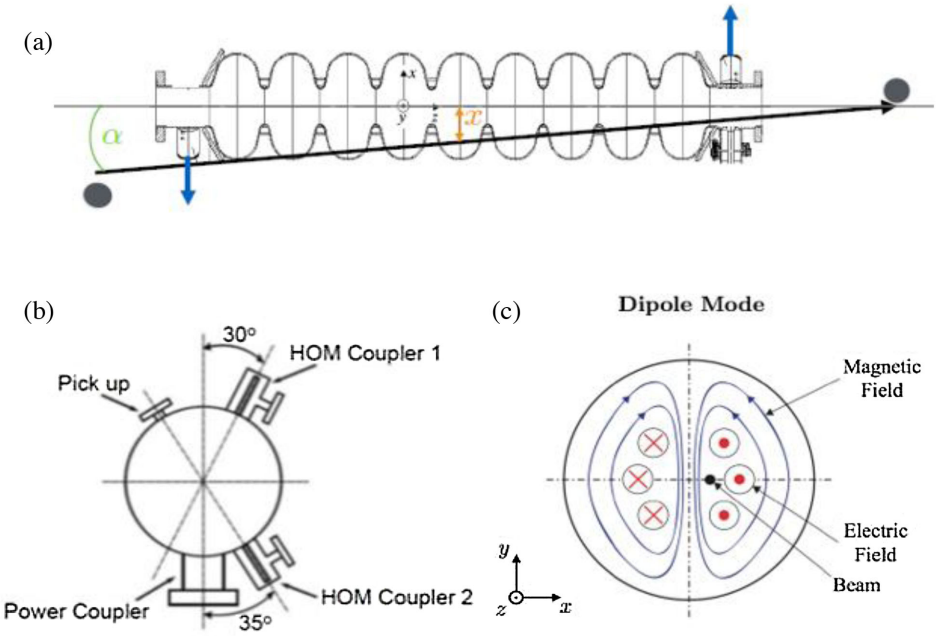

FIG. 2. (a) A schematic of a nine-cell TESLA cavity with HOM couplers shown at each end of the cavity. (b) The azimuthal orientation of the HOM couplers is shown to dampen modes. (c) The induced magnetic and electric dipole modes are shown as one example of each at the lower right for a beam offset in x. The beam is kicked in the direction of the offset initially [14].

going into the first cavity of the cryomodule. Our reference currents were H125 = 1.5 A and V125 = 4.3 A to minimize the HOMs. It is evident that the CM entrance and cavity 1 are off the beamline axis by +12.0 mm in x and +34.4 mm in y using the 2 mrad/A corrector-magnet calibration and the 4-m drift to the CM. There are presumed cavity focusing effects as the beam transits the cavity string so we are more sensitive to the early beam-mode-center offsets. We note that cavities 1, 3, 6 were made by Advanced Engineering Systems (AES) and cavities 2, 4, 5, 7, 8 were made by Research Instruments (RI). Their axial symmetry differences are revealed in the splitting magnitudes of the two polarization components of the dipolar modes seen in the spectral data in Sec. III.

B. The HOM detectors

There are 16 HOM out-couplers within the CM with two per cavity as noted above. The HOM signals were processed by the HOM detector circuits with the Schottky diode output provided online through ACNET, the Fermilab accelerator controls network [6]. The HOM signals are transported from the cavities to the electronics via 1/2″ Heliax cables. Once in the rack, they transition to BNC-terminated RG-58 cables for convenience before entering one of the several analog filter boxes. Since there were different filter boxes being tested, a patch panel was used to quickly switch between cavities and boxes. Unlike the downconverter electronics design with a narrow band filter on the TE_{111} mode used by others [17–19], the HOM detectors' bandpass filters were optimized for two dipole passbands from 1.6 to 1.9 GHz, and the 1.3-GHz fundamental was reduced with a notch filter. The 18 dipolar modes of the nine-cell cavities were previously cataloged by Wanzenberg [20], and we initially hypothesized that most beam transverse kicks would come from the ones with the 10 times higher R/Q values for coupling to the beam such as modes 6, 7, 13, 14, and 30 as listed in Table II. This was borne out by our single-cavity results and the near-resonant effects observed [4].

With the implementation of the two SLAC prototype HOM chassis with eight dipolar channels in total (after commissioning on CC1 [8]), we could cover all eight US or eight DS couplers at one time as schematically shown in Fig. 3. In addition, the hybrid FNAL HOM chassis provided three filtered outputs of two channels on the unused C1 and C8 outputs as indicated. Two 12-channel, 10-bit digitizers provided by FNAL established the link to the ACNET system. The rf BPMs' electronics were configured for bunch-by-bunch beam-position capability with optimized system attenuation for each charge [13].

TABLE II. Summary of the expected TESLA nine-cell cavity dipolar modes' frequencies and R/Q values [20].

Mode number	Frequency (GHz)	R/Q (Ω/cm^2)
MM-6	1.71	5.53
MM-7	1.73	7.78
MM-13	1.86	3.18
MM-14	1.87	4.48
MM-30	2.58	13.16

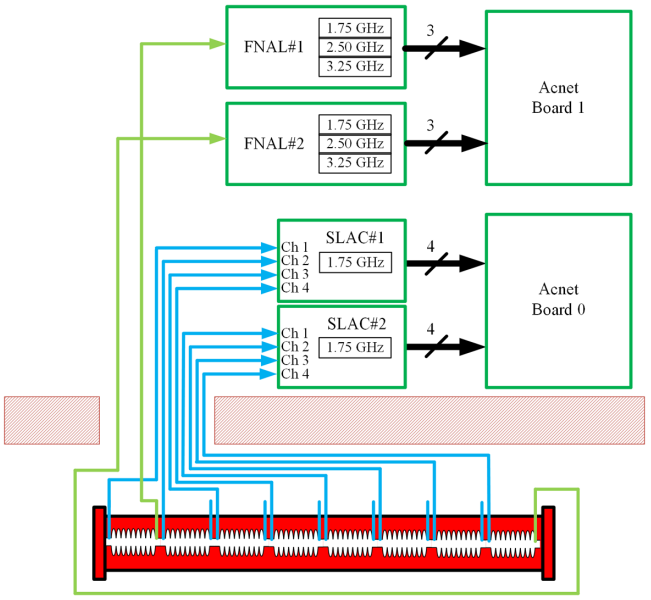

FIG. 3. Schematic of eight channels from the US couplers of eight cavities plus FNAL channels on C1 and C8 DS channels going into the digitizer boards [8].

The schematic of the hybrid HOM filter box used in this set of measurements is shown in Fig. 4. It contains two channels, with each channel having three bandpass filters with passbands of 0.3 or 0.4 GHz centered at 1.75, 2.5, and 3.25 GHz, and an optional 20 dB amplifier controlled by a switch on the front panel. Three of the outputs (one of each frequency band) pass through a Schottky diode to rectify the signal before sending it to the digitizers in the control system. The other three outputs were connected to an 8-GHz analog bandwidth, 20-GS/s, Rohde & Schwarz RTP084 oscilloscope which recorded the HOM signals for further processing offline. The initial dc block in the circuit was to prevent any charge buildup from getting to the 1.3-GHz notch filter. The proximity to the beam harmonics is important when considering the buildup of the HOMs along the bunch train [15].

III. EXPERIMENTAL RESULTS

A. Initial CM2 HOM waveform data: 125 pC/b

An assessment of beam offset in the CM2 cavities was provided by the HOM data, both upstream (US) and downstream (DS) signals. Examples of digitized waveforms using one amplifier (20 dB), which could be displayed in real time during the experiment, are shown in Fig. 5. The CM2 HOM signals were surprisingly ~3x weaker than those of the single cavities, CC1 and CC2, at this charge and at similar cable lengths to the digitizer module. Initially, when no amplifiers were used and with the as-found corrector steering, only the C3 and C4 US HOM waveforms were above the noise. The use of a single wideband amplifier on each channel made all eight signals measurable in Fig. 5 with +1 A (+2 mrad) vertical steering from the reference. The output of the HOM signal depends on the size of the HOM-antenna tip, the gap between antenna and f-part, and the ceramic feedthrough which may have been different in CM2. Steering with corrector V125 located just 4 m before CM2 (see Fig. 1) resulted in the correlated trajectory and HOM signal changes. Our reference currents were H125 = 1.5 A and V125 = 4.3 A. Peak-value data with the H125 corrector current scans are shown in an initial report [8] and in Fig. 6 with the minimum at about H125 = 1.5 A.

B. Bunch-by-bunch rf BPM data: 125 pC/b

We also evaluated the potential long-range wakefield or HOM effects on the beam centroid by using the rf BPM

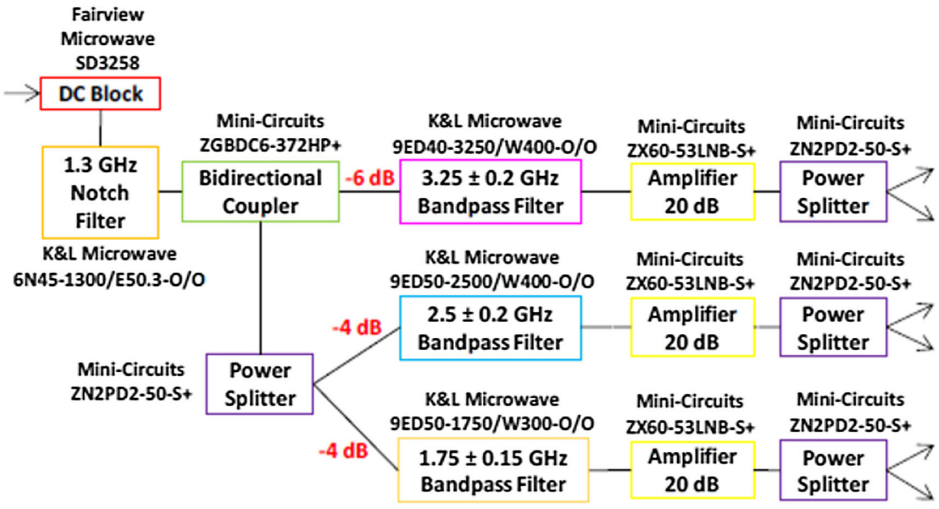

FIG. 4. Schematic of the hybrid HOM filter circuit. The red dB numbers indicate the relative amplitudes of the three channels after the combined bidirectional coupler and power splitter [7].

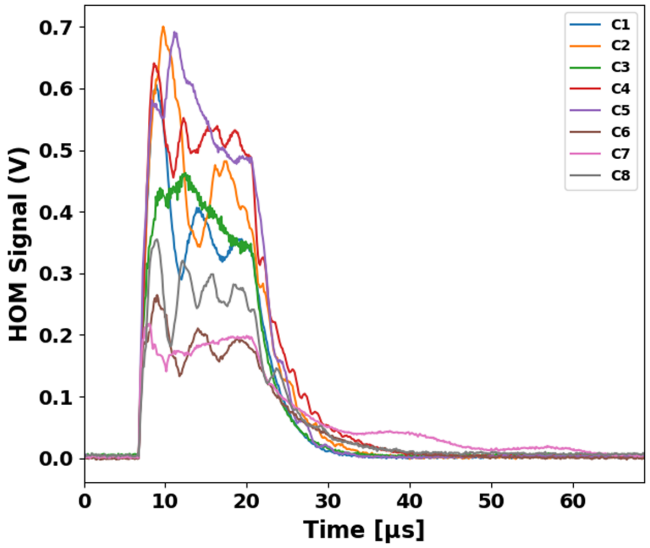

FIG. 5. Initial US HOM waveforms for cavities 1–8 as indicated with one wideband amplifier switched on. All eight Schottky detector signals are now measurable on the same shot. These are the dipolar modes using 50 b over a 16.6 μs temporal extent. Growth of the signal after the first bunch is seen in the leading edge of the waveform. $V125 = +1.0$ A ($+2$ mrad) from the reference.

bunch-by-bunch data after CM2. These data were obtained in an off-normal condition with CC2 tuned 15-kHz off-resonance and powered off. This is discussed elsewhere, but we did identify a residual submacropulse beam-centroid oscillation at ~220 kHz due to CC2 [21].

The beam energy was 25 MeV entering CM2 and 100 MeV exiting. An example of the centroid motion within the 50-micropulse train in a macropulse is shown in Fig. 7 with both noise-reduction and bunch-by-bunch capabilities implemented. The BPM locations are summarized in Table III. B418 is the cold BPM located just after C8 and still within the CM. The first three vertical BPMs after CM2:C8 show an increasing centroid slew correlated with V125 settings which grow to ~500 μm total in B441 at 3.59 m. These data are used in the ML training application described in Sec. IV. Further downstream (64.0 m), we show samples from B480 where a vertical centroid oscillation of $\sim 240 \pm 10$ kHz and slew are seen in Fig. 8 for the two larger (-1 A) V125 corrector values. In this preliminary set, the offset minimum is closer to the -0.5-A case from our reference, with the oscillation amplitude and slew noticeably larger at -1 A (-2 mrad). We attribute this to the combined difference frequencies between the dipolar HOMs and the beam harmonics such as found in Sec. III-E1 and Ref. [4]. We note there is a near resonance in CM:C1 at 1.8775 GHz and a difference frequency of 243.5 kHz which may dominate the observed beam motion since it occurs at the lowest energy in the CM.

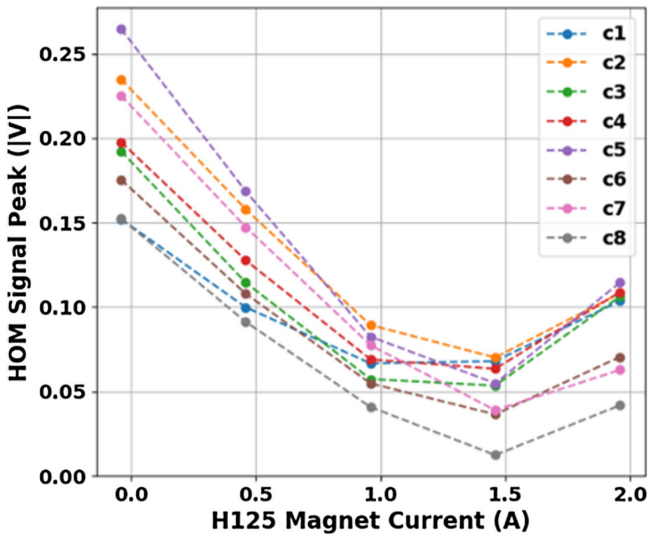

FIG. 6. Initial plots of the CM2 HOM US peak signals vs H125 corrector current values. One amplifier is used in each channel with a charge at 125 pC/b and 50 b. A 300-shot average was used.

C. Integrated HOM Schottky data: 400 pC/b

For the V125 corrector scan, we show the summary results in Fig. 9 for all 16 HOM digitized, frequency-integrated dipolar channels centered at 1.75 GHz. We performed the V125 current scan by setting the corrector current step and acquiring data for the eight US channels at each charge and then for the eight DS channels at each charge. The relative minima are seen for all 16 channels at our reference setting with 400 pC/b, but we observe that the sensitivity to steering is greater for the early cavities than for the DS ones. Cavity 3 (green curve) and C8 (black curve) seem to have elevated minima in the US signals and decreased slopes. Although we had also set the horizontal corrector for local minima of the HOMs, a more complete 2D scan is needed such as in [18] to determine whether this would be due to a horizontal offset of the cavity.

By correlating the readings of the B130 rf BPM located 1 m upstream of the CM with V125 corrector steering and the CM2:C1 US HOMs, one can generate a beam-offset monitor (BOM) plot at the entrance of CM2 with 400 pC/b and 50 b as in Fig. 10. Note the horizontal axis is in mm for this plot. These data were obtained for the first three cavities with one amplifier enabled.

D. Integrated HOM Schottky data: single bunch 10 pC

An important test for the SLAC prototype chassis was deemed to be its ability to detect offsets with a single bunch of 10 pC during commissioning, an order of magnitude below the 100-pC nominal value. Figure 11 shows the signals obtained from all 16 HOM probes with a single 10-pC bunch without changing the accelerator magnet settings. These data were taken after minimizing the signals from the US HOM

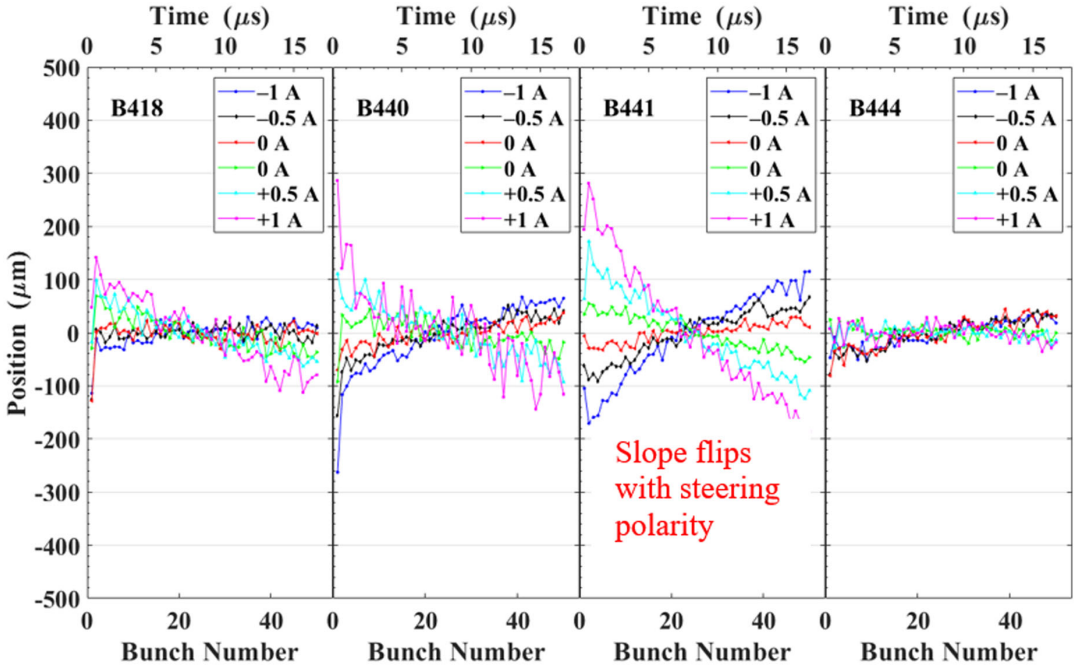

FIG. 7. Submacropulse vertical centroid effects using 300-shot averages in the first four BPM locations after CM2:C8 correlated with V125 settings. This includes the cold BPM denoted B418. The array mean value was subtracted for each curve to make direct comparisons easier. The z-locations are shown in Table III with the maximum centroid slewing seen in B441. The V125 corrector steering angle change is 2 mrad/A.

couplers by hand adjustment of the H/V125 steering magnet settings so we basically had a beam on axis and still enough signals to guide further optimization. Both cascaded amplifiers in each channel were enabled with no added attenuation. This capability may give beam-steering guidance below that of the BPM's charge-sensitivity limit.

E. HOM spectral data: 400 pC/b

1. 1.75-GHz passband data

In a new initiative for us, we operated with a single bunch to explore the detailed spectral information obtainable with a Rohde & Schwarz 20 GS/s oscilloscope [7]. The filtered HOM signals near 1.75 GHz were directly recorded for 15–20 μs after the beam trigger for the 18 dipolar modes in the passband as shown in Figs. 12(a) and 12(b), respectively. Figure 12(c) shows the spectrum near the 1.73-GHz HOM in four cavities, the measured mode values using a network analyzer connected between the two couplers of the cavity (triangles), and the 3-MHz beam harmonics (red circles). The plots in Figs. 12–14 involve only a single bunch, so these HOM peaks will not have any dependence on the vicinity of a beam harmonic. The beam harmonic locations are important for bunch

TABLE III. Summary of the z locations of the BPMs after CM2:C8 noted in the experiments with the PC gun cathode plane as the reference location in column 2 and the cold BPM (B418) as a reference location in the last column.

BPM number	z (m)	Δz (m)
B418	34.71	0.00
B440	37.58	2.87
B441	38.31	3.59
B444	43.74	9.02
B480	98.71	64.00

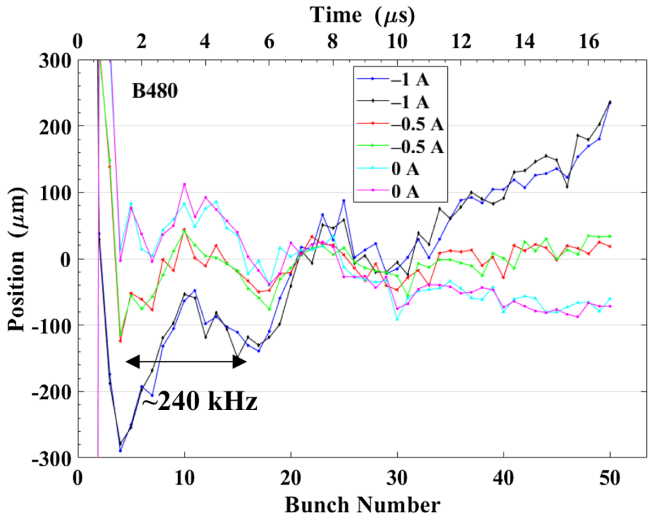

FIG. 8. Examples of the variation with V125 corrector current of the beam vertical centroids bunch by bunch for 50 micropulses and 300-shot averages at B480 (64.0 m downstream of B418). The ~240 kHz centroid oscillation amplitude is observed to be larger for the −1 A (−2 mrad) steering in both cases.

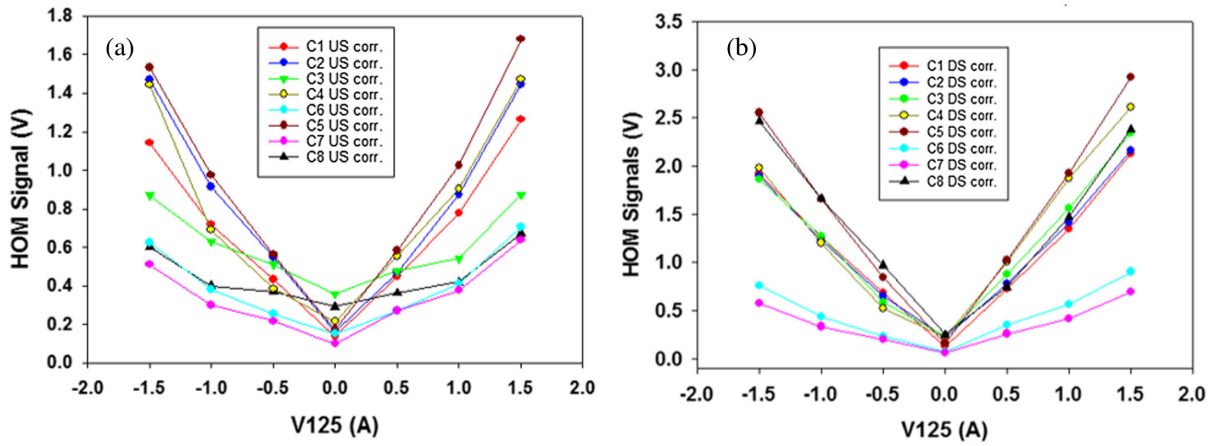

FIG. 9. Measurements of the CM2 (a) US and (b) DS HOM peak signals from the Schottky data. We have identified a reference corrector current setting for our 0.0 A with an actual V125 current value of 4.3 A after scanning for a relative minimum in CM2 US HOM channels. The H125 value was fixed at a reference.

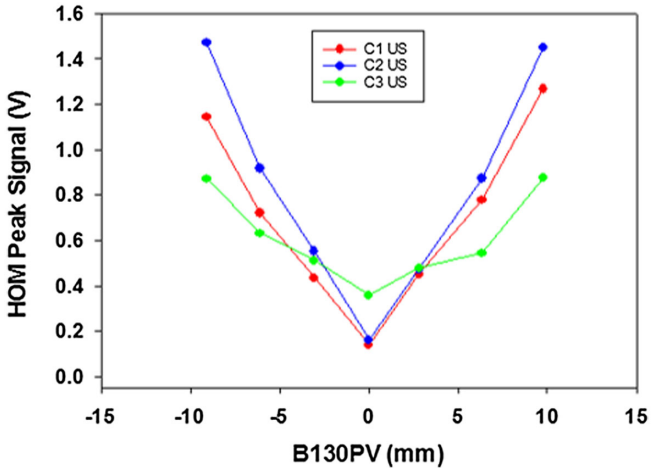

FIG. 10. Beam-offset-monitor plot for B130 with 400 pC/b at entrance to CM2 and the first three cavities. We used 300-shot averages.

trains where leading bunches can impact trailing bunches. Note that each cavity has its own specific frequencies for the modes at a few-MHz level.

Figure 13 shows an example of the FFT of the temporal digital data near 1.72 GHz for CM2:C1 US dipole mode 7. In this case, we resolve the horizontal and vertical polarization components with the horizontal component at 1.7266 GHz clearly changing during the H125 scan from −1 A (−2 mrad) to +1 A (+2 mrad) and the vertical component at 1.7241 GHz changing during the V125 scan. This indicates the mode polarization axes are approximately aligned with the horizontal and vertical spatial axes. The frequency splitting is more than 2 MHz for this Advanced Engineering Systems (AES)-built cavity. The cavity is not axisymmetric evidently.

As another example, we show the CM2:C8 mode 7 near 1.730 GHz in Fig. 14. In this Research Instruments (RI)-built cavity, the frequency splitting is ∼1 MHz, and only

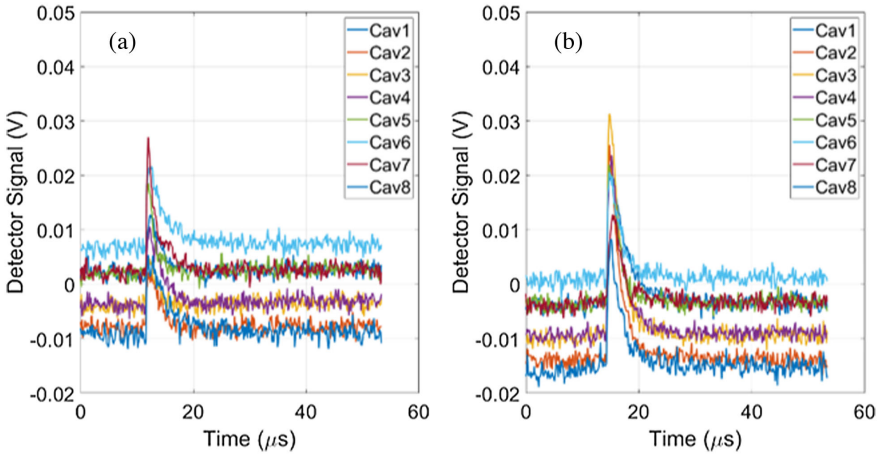

FIG. 11. The output of the SLAC prototype chassis with a single bunch of 10 pC and the beam approximately on axis for (a) US HOMs and (b) DS HOMs (see text). Both cascaded amplifiers are enabled in all channels [8]. We used 300-shot averages and met the experimental objective clearly.

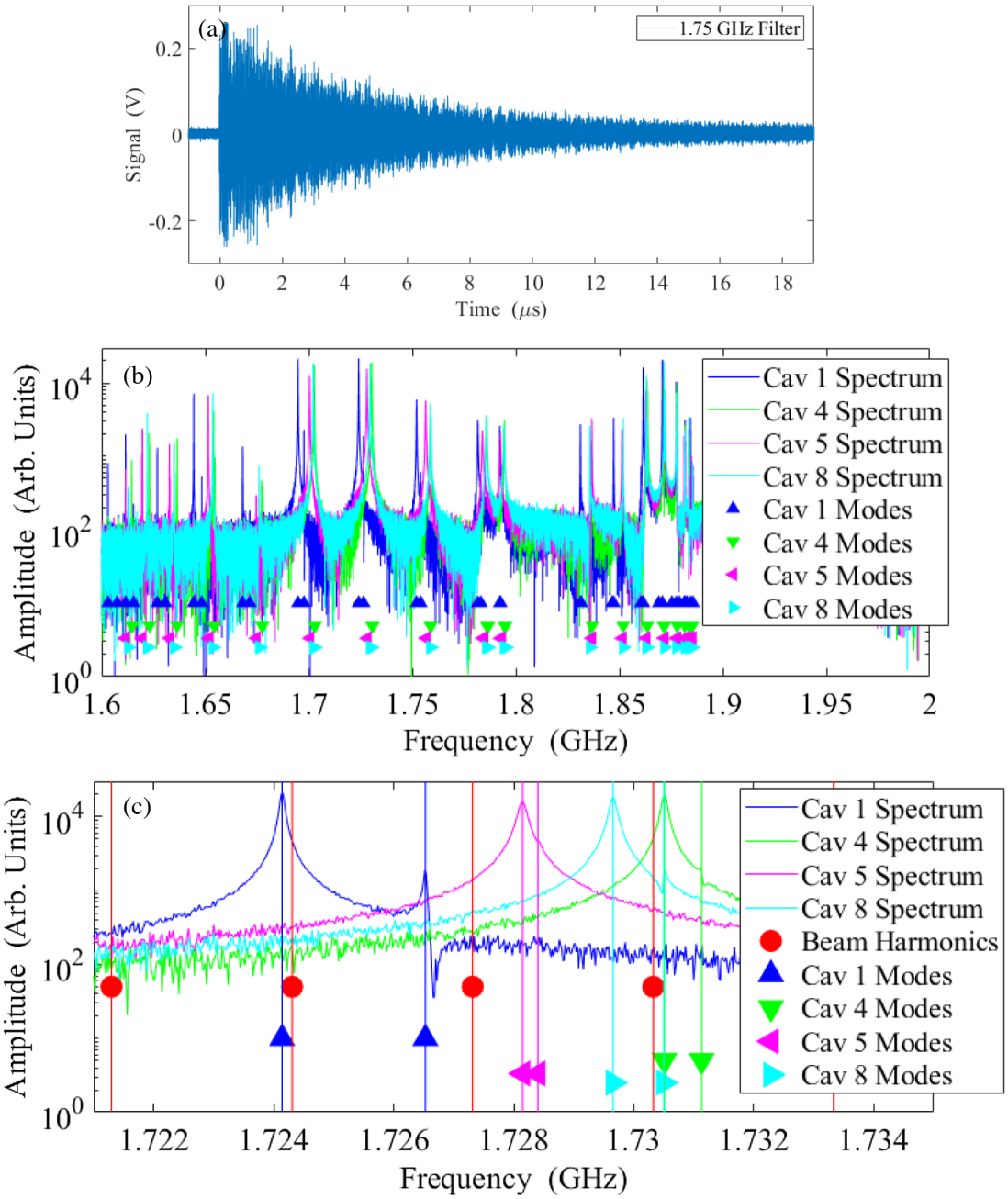

FIG. 12. (a) HOM signals after 1.75-GHz passband filter from cavity 1 of CM2. (b) Spectra of four cavities'18 modes in CM2. (c) Dipolar mode-7 frequencies can vary by up to several MHz in the four sampled cavities of the CM, and the C1 (blue) and C4 (green) cavities have near resonances with the beam harmonics (red circles).

the horizontal component at the higher frequency changes amplitude with the H125 scan values in Fig. 14(a) while only the vertical component at the lower frequency changes amplitude with the V125 scan values in Fig. 14(b). The mode polarization axes are basically aligned with the orthogonal spatial axes here.

To correlate the HOMs with beam steering direction requires the phase of the HOM as well as the magnitude. Extracting the phase requires aligning the time of arrival of the HOM signals. To do this, we (1) measure the stability of the oscilloscope trigger and (2) assume that the first few nanoseconds of signal to arrive from the HOM pickup is the direct signal from the electron bunch passing by the pickup. The trigger for the oscilloscope is derived from the same event trigger as the electron beam photocathode laser. To measure the jitter in the oscilloscope trigger, a different trigger, also derived from the same event trigger source, is fed to the oscilloscope. The variation in the arrival time of

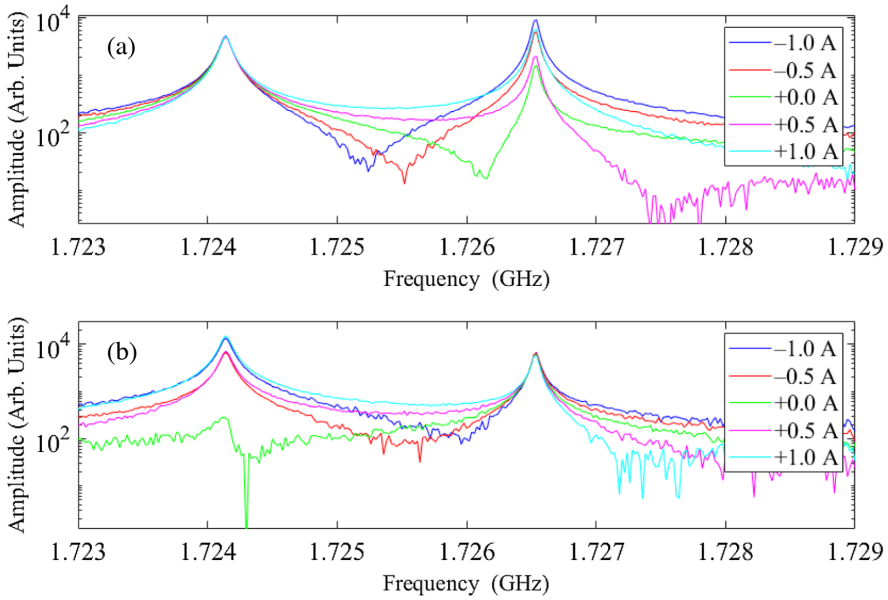

FIG. 13. Horizontal (a) and vertical (b) steering results showing polarization-dependent HOM variations and ∼2-MHz frequency spitting of the two polarizations of dipolar mode 7 in CM2:C1 (AES).

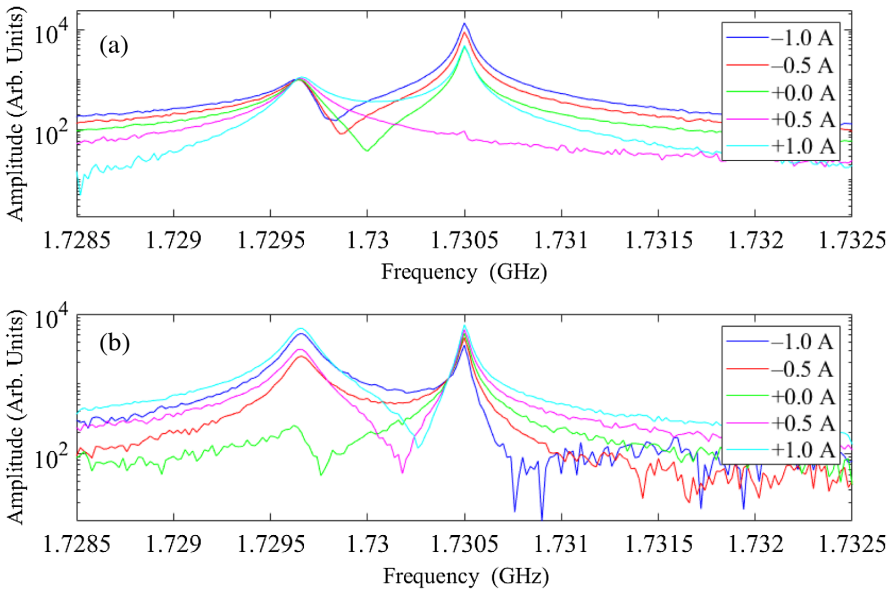

FIG. 14. Horizontal (a) and vertical (b) steering results showing polarization-dependent HOM variations and ∼1-MHz frequency spitting of the two polarizations of dipolar mode 7 in CM2:C8 (RI). Only the vertical polarization component at 1.7297 GHz is responsive to the V125 scan.

this additional trigger, relative to the oscilloscope trigger, is a measure of the trigger jitter. The result of this measurement on 50 trigger pulses is a full-width variation of the trigger time of ∼120 ps or 20% of a 1.7-GHz wavelength. Combining this result with the assumption that the initial signal from the HOM pickup is from the beam allows us to correct the trigger jitter by shifting the HOM signals to align the time signals using one of the initial peaks.

Figure 15 shows the start of the HOM signals for various beam trajectories from a single pickup within a single cavity (a) before and (b) after aligning using the peak at what we have arbitrarily called a time of 0 ns. The spread in peaks before aligning them matches the previously measured jitter in the trigger signal giving us some confidence in the technique. In Fig. 16, we see the mode 7 amplitude in CM2:C1 for the V125 corrector scan. In this case, we

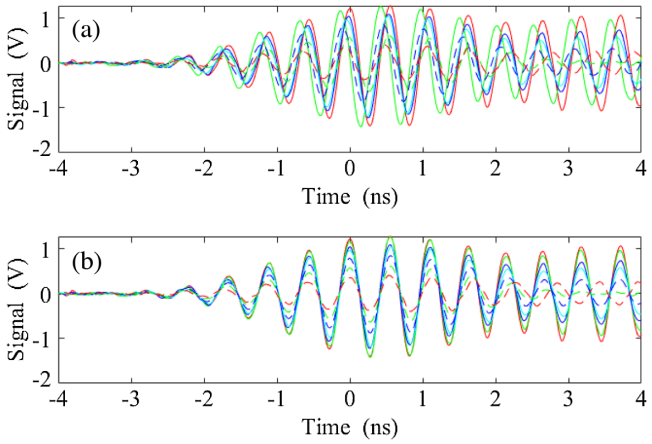

FIG. 15. HOM signals from the oscilloscope. The curves are different beam trajectories from the same coupler and cavity. (a) These signals are after filtering and include all the modes within the 1.75-GHz bandpass filter. (b) Same signals, but after aligning them in time using the peak at 0 ns.

applied the phase information so we extract the sign of the vertical steering. This confirms our assessment from the HOM Schottky data for minimized HOM dipolar signals shown in a previous Sec. III C, and the reference steering. We observed similar results on modes 6, 7, 13, and 14 for cavities 1, 4, 5, and 8 although the polarization component frequency splittings varied.

2. 2.5-GHz passband data

The objective of acquiring data in this regime was to determine whether the dipolar mode 30 at ~2.578 GHz with a large coupling value reported in Refs. [20,22] could be excited in CM2 and show effects on the submacropulse beam-centroid motion downstream of the CM. We had previously found evidence for its role in CC1 [4]. This mode

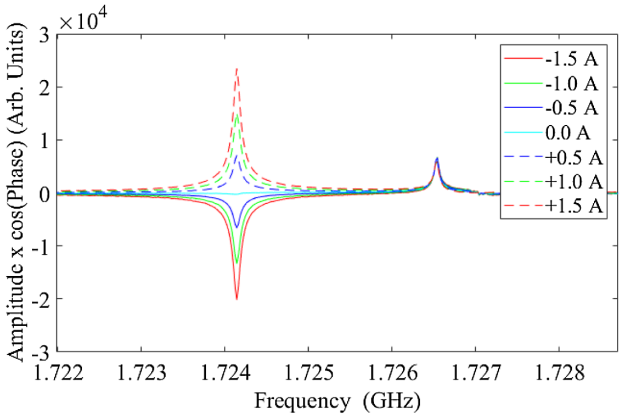

FIG. 16. "Signed" spectra of ~1.72 GHz mode showing the V125 vertical corrector steering effects on the dipolar mode 7 amplitude in C1. The reference 0.0-A setting is confirmed with the low mode amplitude observed in this and for other dipolar modes.

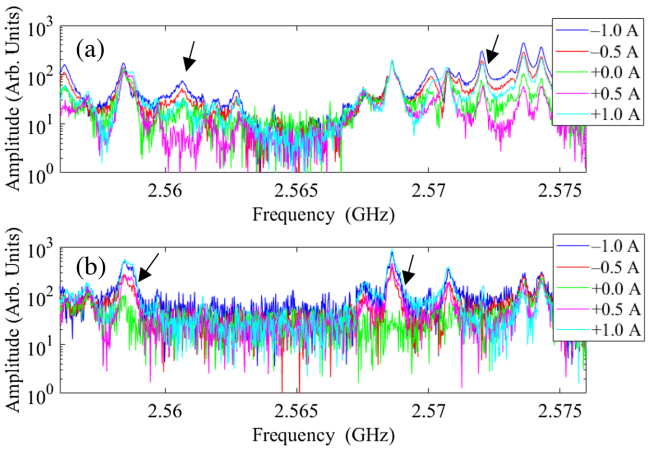

FIG. 17. Horizontal (a) and vertical (b) steering results showing polarization-dependent HOM variations in several modes from 2.555 to 2.575 GHz in CM2:C1 as indicated by the arrows.

would need to be near resonant with a beam harmonic to have much effect based on those studies. The frequency-integrated Schottky data for CM2:C1 US HOM showed a relatively strong signal, but no correlation with the steering and other dipolar HOMs. We suspect some monopole modes in this broad passband dominate the total signal and obscure the dipolar mode effect. However, the high-resolution frequency data in Fig. 17 do show modes whose amplitudes are sensitive to either the horizontal (H) or vertical (V) steering at 2.558 (V), 2.561 (H), 2.568 (V), and 2.572 (H) GHz which are indicated by the small black arrows in Figs. 17(a) and 17(b).

3. 3.25-GHz passband data (integrated)

The objective of studies in this 3.25-GHz regime was to assess the quadrupole modes reported in a TESLA-type cavity [20]. The quadrupole modes are expected to be excited by off-axis charges inside the cavities [20]. In Fig. 18(a), we show that the C1 US HOM signal remains the same to a few mV (although nonzero) during the V125 scan while the C8 US HOM indicates some changes in excitation of the modes in this passband with V125 corrector steering by more than ±1 A or ±2 mrad. In Fig. 18(b), we show the DS HOMs are excited for these two cavities in this passband. Both C8 US and C8 DS HOM signals show a quadratic-like dependence on beam offset presumably due to the HOM quadrupole fields excited in this passband within the cavity. Further studies are warranted. The signals for each corrector value were averaged over 300 shots with 250 pC/b and 50 b.

F. Discussion of experimental results

Overall, our assessments are that dipolar modes 6, 7, 13, and 14 are the strongest ones in coupling to the beam based on the sampling of four of the eight cavities with near resonances to the beam harmonics in most of them.

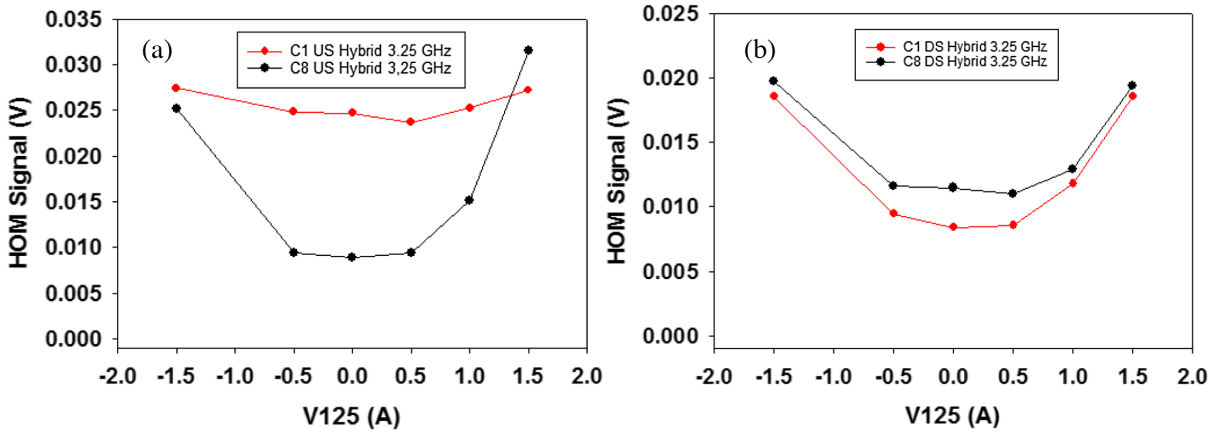

FIG. 18. A comparison of the 3.25-GHz signals in the (a) CM2:C1 US HOM (red data) and the C8 US HOM (black data) and (b) C1 DS and C8 DS during the V125 scan. The data exhibit a quadratic variation with beam offset symptomatic of a quadrupole field effect. The data are based on 300-shot averages.

We expect that the submacropulse beam centroid motion at ~240 kHz and ~500-μm slew in Fig. 8 is the superposition of all of these time-varying HOM fields during the macropulse time scale, but the near resonance in CM:C1 is notable. We proposed that by combining the rf BPM data with the HOM signals, one could have input to minimize the emittance dilution. As a development task, we consider the possibility of a machine-learning-training application for this in the next section. We note that the beam energy was 25 MeV entering the CM, and the offset effects at 1 MeV into the LCLS-II injector CM could be serious with zero gradients planned in C2 and C3 (increasing these gradients should partly mitigate the effects). The exit energy at FAST of 100 MeV is close to the 90-MeV exit energy at the LCLS-II injector CM. Although our integrated dipolar signals have a slightly broader minimum than our individual mode analyses, they provide online results for fast commissioning and ML training and are confirmed by the signed spectral data. We used the normal FAST linac 3-MHz rate compared to the 1-MHz rate at LCLS-II and the 4.5-MHz rate at the EuXFEL, but the effects should be similar within the pulse train. The effects of the cw pulse train at LCLS-II are to be investigated.

IV. MACHINE-LEARNING TRAINING

Machine learning is undergoing a renaissance in a wide variety of applications due to larger computational resources, advanced theoretical models, and successful practical applications during the last years. Particle accelerators are part of this resurgence of ML due to developments of new system modeling techniques, virtual instrumentation/diagnostics, tuning and control schemes, surrogate models, among others [23]. In this section, we evaluate a neural network (NN) model for bunch-by-bunch centroid slewing prediction and its application in an ML-based optimization and model construction for HOM signal level reduction and emittance preservation. A NN model that can predict transverse beam position, based on HOM signals, can be used by a controller to tune the steering magnets' currents to minimize beam offset and HOM signal levels, therefore minimizing emittance dilution. The effects of emittance dilution are especially crucial in the first LCLS-II CM after the injector, where the beam energy will be less than 1 MeV. The results presented here will inform the commissioning plan for the LCLS-II injector CM.

A. Data source and structure

Our new experimental results in Sec. III, Fig. 7 showed a correlation between the electron beam–induced cavity HOM signal levels and bunch-by-bunch centroid slewing and oscillation at the first 4 of the 11 BPMs located downstream of the CM [24]. Thus, by reducing HOM signals and bunch-by-bunch centroid slewing downstream of the CM, one can mitigate emittance dilution. In principle, a NN control policy could be used for this purpose.

Waveform examples of US HOMs for all eight cavities are shown in Fig. 5. Although several features can be extracted from each of these waveforms (peak, integral, rise time, oscillation frequency, and decay time), we decided to use the peak value as a representative number. Averaging the peak value over 300 shots, the relation between the V125 corrector current and HOM signal peaks at 400 pC/b and 50 bunches was shown in Fig. 9. The evolution of the relative beam centroid position as measured by B441PV (a BPM located ~3.59 m DS of the CM) over a 250-pC/b beam with 50 bunches is shown in Fig. 19 for multiple values of V125 corrector current and H125 at its reference value.

With these results, we can see how both HOM signal peaks and centroid slews are proportional to the corrector current (i.e., beam off-axis). In principle, we can train a NN to predict the centroid slew based on the HOM signal peaks (or the integrals).

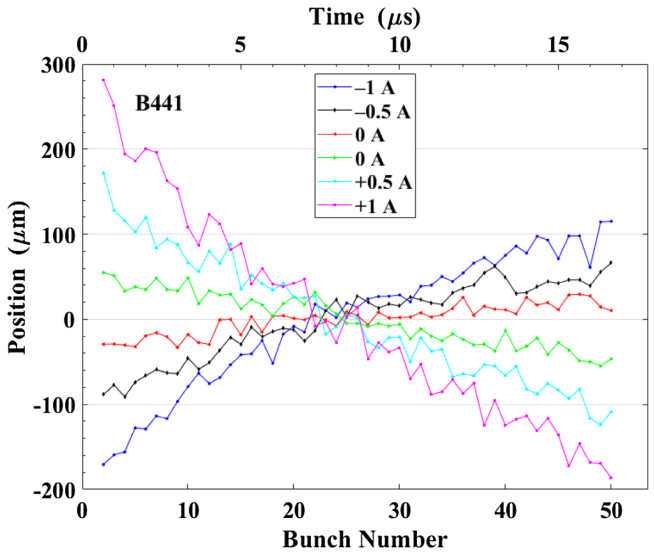

FIG. 19. Submacropulse vertical beam centroid motion at B441PV located 3.59 m downstream of the CM. This is the third panel of Fig. 7 shown with an adjusted vertical scale for the reader's convenience.

B. Neural network model

With our ML model, we aim to make fast inferences from many signals; therefore, we chose a NN and a supervised learning approach. A NN can learn the mapping between inputs and outputs using many connected processing units called neurons or nodes, which are grouped into layers. With supervised learning, the NN learns the input/output mapping by comparing the predicted output with the real output. Background on NN can be found in Ref. [25].

An NN was trained to predict the centroid motion's standard deviation as measured by multiple BPMs (B440PV/PH and B441PV/PH) over beams of 50 bunches, for several values of bunch charge and H/V125 corrector currents. The inputs to the NN are the US and DS HOM signal peaks as measured by the SLAC HOM detectors. The training data included measurements for beam charges of 200 and 100 pC/b, and H/V125 corrector currents from −1.0 A to +1.0 A from the reference current, with 0.5-A current steps. At each beam configuration, signals for 300 shots were captured. The result is a dataset with 6000 data points.

The NN architecture consisted of a normalization layer followed by six hidden layers (four layers of 100 nodes followed by two layers of 64 nodes). The normalization layer was added at the beginning of the NN to improve the stability and performance of the model and to prevent the saturation of neurons. Manual tuning of the number of layers and nodes, known as hyperparameters, was performed by training the NN while changing hyperparameter values until acceptable results were obtained. Each hidden layer used the hyperbolic tangent activation function.

TABLE IV. NN performance results.

BPM	Train MAE [μm]	Val MAE [μm]	Test MAE [μm]	Test MAPE [%]
B440PV	41.42	41.98	42.82	9.76
B440PH	29.82	30.46	30.54	8.20
B441PV	18.98	19.26	19.50	8.40
B441PH	20.89	21.43	21.62	8.44

An 80-20 split was used for the training (4800 data points) and test datasets (1200 data points). From the training data set, 20% was used for validation. An early stop was implemented to save resources and computation time.

C. Training results

The performance of the model was evaluated in terms of the mean absolute error (MAE) and the mean absolute percent error (MAPE), calculated with the following equations:

$$MAE = \text{mean}(|y_{true} - y_{pred}|)$$

$$MAPE = \text{mean}\left(\left|\frac{y_{true} - y_{pred}}{y_{true}}\right|\right) \cdot 100\%$$

Both quantities are a measure of how far the predictions are from the real values and represent the average magnitude of error for the predictions of our model. MAPE is conveniently expressed in percentages.

Computing resources of the SLAC Shared Scientific Data Facility (SDF) were used to perform the NN training [23]. The results are shown in Table IV. The accuracy of the prediction of the standard deviation of the bunch-by-bunch centroid slew is about 8% for all BPMs shown. A representative histogram of the test data set MAPE for B441PV (vertical) is shown in Fig. 20.

The performance of the NN model for predictions of B441PV standard deviation over the test dataset is shown in

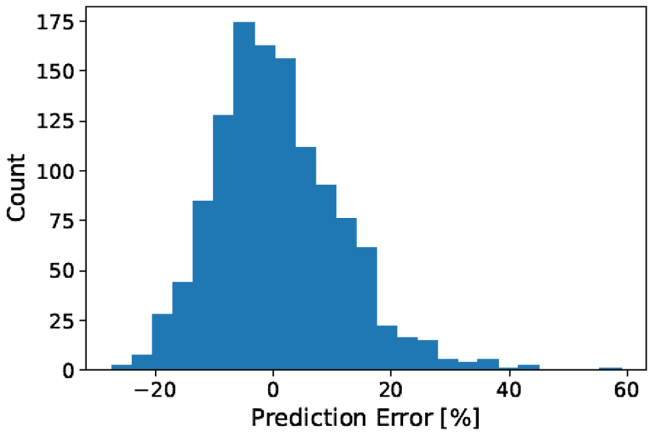

FIG. 20. Histogram of prediction errors for B441PV.

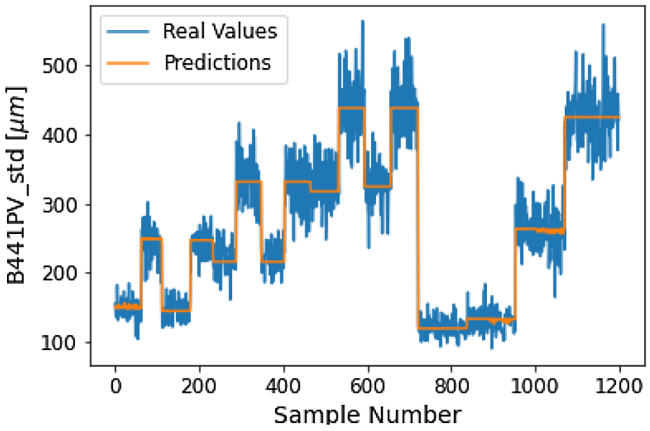

FIG. 21. NN model predictions and real values for B441PV.

Fig. 21. The x-axis represents the test dataset, which consists of 1200 data points (20% of the total dataset size). The predictions (gold) appear centered in the BPM real values (blue). The groups in Fig. 19 represent BPM measurements over the same beam and corrector configuration (i.e., fixed bunch charge and H/V125 corrector currents). These groups consist of ∼60 data points since we took 300 shots for each beam and corrector configuration. The NN model is capable of predicting the average bunch-by-bunch centroid slew's standard deviation for a given beam and corrector configuration. However, it is not accurate when predicting the exact value. This may be related to the noise on the BPM measurements and the low charge. Having the average bunch-by-bunch centroid slew's standard deviation might be enough when designing a controller based on these predictions. For a given charge, the minimum centroid slew and oscillation would correspond to the minimum standard deviation of the positions.

Data with the unprecedented correlation between beam steering, US and DS HOM signals, and BPM measurements showing bunch-by-bunch centroid slew after a TESLA-type CM at FAST have been used to train a NN model. Results show that the NN model is capable of predicting the centroid slew's standard deviation with about 8% accuracy. These are encouraging results toward developing an ML-based controller for HOM reduction and emittance preservation for the LCLS-II project at SLAC. Our next steps include the development of the controller using an inverse model of the NN developed in this research, i.e., a NN that can predict HOM signals for a given beam offset. We plan to compare our ML-based model dealing with a pulse train's effects to classical feedback techniques such as previously used on a single HOM for a single bunch [26]. The ML training should consider beam energy at each cavity, near resonances of a HOM frequency to a beam harmonic, and cavity misalignment information. We also plan to explore adaptive learning, Gaussian processes [27], and Gaussian process-based Bayesian optimization.

V. SUMMARY

In summary, we have performed our first comprehensive study of the beam dynamics associated with HOMs in a TESLA-type cryomodule at the FAST/IOTA facility. We used rf BPM bunch-by-bunch data, integrated HOM dipole mode responses online, and high-resolution spectral measurements processed offline showing phase and frequency splitting of the polarization components of key modes. These were used to support HOM minimization and concomitant emittance-dilution reduction. This has been augmented by initial ML training with these data in support of this objective and for informing the commissioning of the LCLS-II injector with < 1 MeV beam injected into the first CM. These results also could have relevance to the EuXFEL injector where ∼6-MeV beam enters the first CM or to future high-current synchrotron light sources using such technology [28]. It is hoped that the data may be used to benchmark a simulation of such dynamics for a full cryomodule in the future.

ACKNOWLEDGMENTS

The Fermilab authors acknowledge the technical support of B. Fellenz; the support of C. Drennan, A. Valishev, D. Broemmelsiek, G. Stancari, and M. Lindgren; all in the Accelerator Division at Fermilab; discussions with V. Yakovlev and measurements with the CM2 network analyzer by A. Lunin, both of the Applied Physics and Superconducting Technology Division at Fermilab. The SLAC/NAL authors acknowledge the support of J. Schmerge (Superconducting Linac Division, SLAC). The Fermilab authors also acknowledge the support of Fermi Research Alliance, LLC under Contract No. DE-AC02-07CH11359 with the U.S. Department of Energy. The SLAC/NAL authors acknowledge support under Contract No. DE-AC02-76SF00515 with the U.S. Department of Energy.

[1] H. Weise and W. Decking, Commissioning and first lasing of the European XFEL, in *Proceedings of the 38th International Free Electron Laser Conference (FEL'17), Santa Fe, NM, USA, 2017* (JACoW, Geneva, Switzerland, 2017), pp. 9–13, 10.18429/JACoW-FEL2017-MOC03.

[2] P. Emma, Status of the LCLS-II FEL Project at SLAC, in *Proceedingsof the 38th International Free Electron Laser Conference (FEL'17), Santa Fe, NM, USA, 2017* (JACoW, Geneva, Switzerland, 2017), MOD01.

[3] J. T. Seeman *et al.*, Transverse wakefield control and feedback in the SLC Linac, in *Proceedings of the 1987 Particle Accelerator Conference* (IEEE, Washington, DC, USA), pp. 1349–1353.

[4] A. H. Lumpkin, R. Thurman-Keup, D. Edstrom, J. Ruan, N. Eddy, P. Prieto, O. Napoly, B. E. Carlsten, and K. Bishofberger, Submacropulse electron-beam dynamics correlated with higher-order modes in Tesla-type

superconducting rf cavities, Phys. Rev. Accel. Beams **21**, 064401 (2018).

[5] A. H. Lumpkin, R. M. Thurman-Keup, D. Edstrom, and J. Ruan, Submicropulse electron-beam dynamics correlated with short-range wakefields in Tesla-type superconducting rf cavities, Phys. Rev. Accel. Beams **23**, 054401 (2020).

[6] M. Church *et al.*, The ASTA User Facility Proposal, Fermi National Accelerator Laboratory, Batavia, IL, Report No. Fermilab-TM-2568, 2013.

[7] R. Thurman-Keup *et al.*, Observation of polarization-dependent changes in higher-order mode responses as function of transverse beam position in Tesla-type cavities at FAST, in *Proceedings of the 12th International Particle Accelerator Conference, IPAC-2021, Campinas, SP, Brazil* (JACoW, Geneva, Switzerland, 2021), MOPAB232.

[8] J. Sikora *et al.*, Commissioning of the LCLS-II prototype HOM detectors on TESLA-type cavities at FAST, in *Proceedings of the 12th International Particle Accelerator Conference, IPAC-2021, Campinas, SP, Brazil* (JACoW, Geneva, Switzerland, 2021), MOPAB323.

[9] Pei Zhang, Nicoleta Baboi, Roger M. Jones, Ian R. R. Shinton, Thomas Flisgen, and Hans-Walter Glock, A study of beam position diagnostics using beam-excited dipole modes in third harmonic superconducting cavities at a free-electron laser, Rev. Sci. Instrum. **83**, 085117 (2012).

[10] Jorge Diaz-Cruz, A. Edelen *et al.*, Machine learning training for HOM reduction and emittance preservation in a TESLA-type cryomodule at FAST, in *Proceedings of the 12th International Particle Accelerator Conference, IPAC-2021, Campinas, SP, Brazil* (JACoW, Geneva, Switzerland, 2021), MOPAB289.

[11] F. Zhou *et al.*, LCLS-II injector physics design and beam tuning, in *Proceedings of the International Particle Accelerator Conference, IPAC-2017, Copenhagen, Denmark, 2017* (JACoW, Geneva, Switzerland, 2017), TUPAB138.

[12] J. Ruan, M. D. Church, D. R. Edstrom, T. R. Johnson, and J. K. Santucci, Commissioning of the Drive Laser System for Advanced Superconducting Test Accelerator, in *Proceedings of the 4th International Particle Accelerator Conference, IPAC-2013, Shanghai, China, 2013* (JACoW, Shanghai, China, 2013), pp. 3061–3063, WEPME057.

[13] N. Eddy *et al.*, High resolution BPM upgrade for the ATF damping ring at KEK, in *Proceedings of the 10th European Workshop on Beam Diagnostics and Instrumentation for Particle Accelerators, Hamburg, Germany, 2011* (DESY, Hamburg, 2011).

[14] Thorsten Hellert, Liang Shi, and Nicoleta Baboi, Progress on higher-order-mode-based cavity misalignment measurements at FLASH, in *Proceedings of the DESY Seminar, Hamburg Germany*, 2017, https://flash.desy.de/sites2009/site_vuvfel/content/e870/e257076/infoboxContent257077/Hellert_FELSeminar_170711_FEL_HOM.pdf.

[15] Rainer Wanzenberg, HOMS in the TESLA 9-cell cavity, in *Proceedings of the SPL HOM Workshop*, CERN, 2009, https://indico.cern.ch/event/57247/contributions/1212325/attachments/988671/1405921/TESLAcavityHOM.pdf.

[16] Junhao Wei, Nicoleta Baboi, Wolfgang Ackermann, and Thorsten Hellert, Cavity tilt measurement using beam excited higher order mode signals at the Free Electron Laser FLASH, Nucl. Instrum. Methods Phys. Res., Sect. A **1000**, 165246 (2021).

[17] J. Frisch, N. Baboi, N. Eddy, and S. Nagaitsev, Electronics and algorithms for HOM based beam diagnostics, *AIP Conf. Proc.* 868, 313 (2006).

[18] T. Hellert, N. Baboi, and L. Shi, Higher order mode based cavity misalignment measurements at the free-electron laser FLASH, Phys. Rev. Accel. Beams **20**, 123501 (2017).

[19] J. Wei, N. Baboi, and L. Shi, Transverse diagnostics based on dipole mode signal fitting method in TESLA- type accelerating cavities at the free-electron laser FLASH, Phys. Rev. Accel. Beams **22**, 082804 (2019).

[20] R. Wanzenberg, Monopole, dipole and quadrupole pass-bands of the TESLA 9-cell cavity, TESLA Report No. 2001–33, Hamburg, Germany, 2001.

[21] A. H. Lumpkin *et al.*, Observations of long-range wake-field effects generated by an off-resonance TESLA-type cavity, in *Proceedings of the 12th International Particle Accelerator Conference, IPAC-2021, Campinas, SP, Brazil* (JACoW, Geneva, Switzerland, 2021), TUPAB272.

[22] S. Fartoukh *et al.*, Evidence for a strongly coupled dipole mode with insufficient damping in TTF first accelerating module, in *Proceedings of the 18th Particle Accelerator Conference, New York, 1999*(IEEE, New York, 1999), p. 922.

[23] A. Edelen *et al.*, Opportunities in machine learning for particle accelerators, arXiv:1811.03172.

[24] A. H. Lumpkin *et al.*, Investigations of long-range wake-field effects in a Tesla-type cryomodule at FAST, in *Proceedings of the 12th International Particle Accelerator Conference, IPAC-2021, Campinas, SP, Brazil* (JACoW, Geneva, Switzerland, 2021), TUPAB274.

[25] S. Haykin, *Neural Networks and Learning Machines*, 3rd ed. (Prentice-Hall, NJ, 2009).

[26] Josef Frisch *et al.*, High precision SC cavity diagnostics with HOM measurements in *Proceedings of the 10th European Particle Accelerator Conference (EPAC 06), Edinburgh, Scotland, 2006* (EPS-AG, Edinburgh, Scotland, 2006), TUYPA02.

[27] C. E. Rasmussen and C. K. I. Williams, *Gaussian Processes for Machine Learning* (MIT Press, Cambridge, MA, 2006).

[28] A. V. Vélez, H.-W. Glock, P. Goslawski, A. Jankowiak, J. Knobloch, A. Neumann, M. Ries, and G. Wüstefeld, BESSY VSR: A novel application of SRF for synchrotron light sources, in *Proceedings of the 17th International Conference on RF Superconductivity, Whistler, BC, Canada, 2015* (JACoW, Geneva, Switzerland, 2015), pp. 462–466, TUAA03, 10.18429/JACoW-SRF2015-TUAA03.